INTERNATIONAL JOURNAL FOR NUMERICAL METHODS IN FLUIDS, VOL. 12, 835–857 (1991)

A CONSISTENT BOUNDARY ELEMENT METHOD FOR FREE SURFACE HYDRODYNAMIC CALCULATIONS

DANIEL E. MEDINA* AND JAMES A. LIGGETT

School of Civil and Environmental Engineering, Cornell University, Ithaca, NY 14853, U.S.A.

AND

RICHARD A. BIRCHWOOD AND KENNETH E. TORRANCE

Sibley School of Mechanical and Aerospace Engineering, Cornell University, Ithaca, NY 14853, U.S.A.

SUMMARY

Free surface phenomena are described by equations that exhibit two types of non-linearities. The first is inherent to the equations themselves and the second is caused by the application of boundary conditions at a free surface at an unknown location. Numerical calculations usually do not specifically recognize the second non-linearity, nor treat it in a fashion consistent with the more obvious non-linearities in the boundary conditions. A consistent formulation is introduced in the present paper. The field equation is integrated and the free surface boundary conditions are applied on the unknown geometry by means of appropriate series expansions. The consistent formulation introduces improvements in accuracy and computing speed. The method is demonstrated on several hydrodynamic free surface problems and an error analysis is included.

KEY WORDS Boundary element Free surface Hydrodynamic

1. INTRODUCTION

The boundary element method (BEM) has been successfully applied to analyse phenomena involving a free surface such as groundwater flow and hydrodynamic problems. When compared with finite element or finite difference schemes, the major advantage provided by the BEM is the ease in regridding the geometry of the flow region. The equations describing free surface problems are non-linear by themselves, but additional non-linear effects arise from the fact that boundary conditions must be applied at a surface whose location is unknown. Usually this difficulty is circumvented by neglecting the change in the geometry, applying the conditions at the previously computed position of the surface and iterating to refine the new geometry. This method generally requires small time steps to preserve accuracy. For two-dimensional groundwater flow, Liggett[1] derived a formulation of the BEM that explicitly recognizes the non-linear effect introduced by the unknown position of the free surface. The purpose of this paper is to extend the concept to the more complex case of hydrodynamic problems.

* Present address: Department of Civil Engineering, Northeastern University, Boston, MA 02115, U.S.A.

0271–2091/91/090835–23$11.50

Received January 1990
Revised July 1990

2. GOVERNING EQUATIONS

Consider the general two-dimensional hydrodynamic problem shown in Figure 1. Under the assumptions of inviscid and irrotational flow of an incompressible fluid, the flow field can be defined by means of a velocity potential Φ:

$$\mathbf{V}=\nabla\Phi, \tag{1}$$

where $\mathbf{V}$ is the velocity vector. Introducing the continuity equation, it follows that the potential must be harmonic:

$$\nabla^2\Phi=0. \tag{2}$$

The boundary condition on the walls can be written as

$$\frac{\partial\Phi}{\partial n}=q(x, z, t), \tag{3}$$

where q and n are the outward-directed flow velocity and unit vector, both normal to the walls. Radiation boundary conditions are not included in the analysis.

On the free surface there are two conditions that must be satisfied. The first is the kinematic boundary condition derived from the assumption that the surface is a material line. Hence if the surface is given by

$$z=\eta(x, t), \tag{4}$$

the assumption translates into

$$\frac{\partial\eta}{\partial t}+\frac{\partial\Phi}{\partial x}\frac{\partial\eta}{\partial x}=\frac{\partial\Phi}{\partial z}. \tag{5}$$

The dynamic boundary condition establishes continuity of the normal stresses at the free surface and is expressed by Bernoulli's equation:

$$\frac{\partial\Phi}{\partial t}+\frac{1}{2}\left[\left(\frac{\partial\Phi}{\partial x}\right)^2+\left(\frac{\partial\Phi}{\partial z}\right)^2\right]+g\eta+\frac{\sigma}{\rho}\frac{1}{R}=0, \tag{6}$$

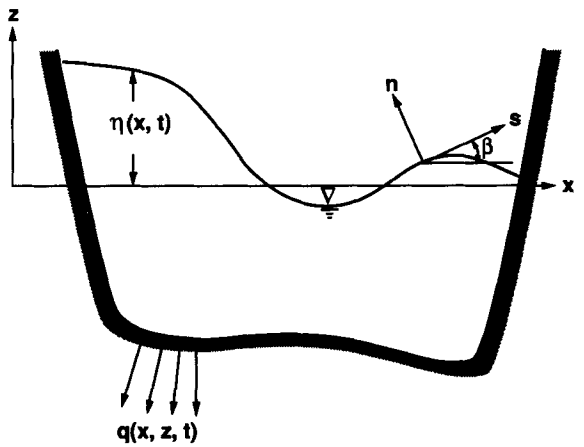

Figure 1. Definition sketch for the two-dimensional hydrodynamic problem

where ρ is the density of the fluid, σ is the surface tension, g is the gravitational acceleration and R is the radius of curvature given by $R^{-1} = -\eta_{xx}/[(\eta_x)^2 + 1]^{3/2}$.

Choosing L as a characteristic length and defining the dimensionless variables

$$x^* = x/L, \qquad z^* = z/L, \qquad \eta^* = \eta/L,$$
$$t^* = t\sqrt{(g/L)}, \qquad V^* = V/\sqrt{(gL)}, \qquad \Phi^* = \Phi/\sqrt{(gL^3)}, \tag{7}$$

the governing equation and the boundary conditions reduce to

$$\mathbf{V}^* = \nabla\Phi^*, \tag{8}$$

$$\nabla^2\Phi^* = 0, \tag{9}$$

$$\frac{\partial\Phi^*}{\partial n^*} = q^*(x^*, y^*, z^*), \tag{10}$$

$$\frac{\partial\eta^*}{\partial t^*} = \frac{1}{\cos\beta}\frac{\partial\Phi^*}{\partial n^*}, \tag{11}$$

$$\frac{\partial\Phi^*}{\partial t^*} + \frac{1}{2}\left[\left(\frac{\partial\Phi^*}{\partial x^*}\right)^2 + \left(\frac{\partial\Phi^*}{\partial z^*}\right)^2\right] + \eta^* + \frac{1}{We^2}\frac{1}{R^*} = 0, \tag{12}$$

where the Weber number appears and is defined as

$$We^2 = \rho g L^2/\sigma. \tag{13}$$

The angle β denotes the slope of the free surface measured from the horizontal and is positive in the counterclockwise direction. In the subsequent discussion the asterisks will be dropped for simplicity.

The equations can be further modified by the inclusion of a preferred direction along which the surface nodes are allowed to move. Figure 2 shows the surface at time level k and a node that is to be moved along the z'-axis to a position on the surface at time level $k+1$. The choice of the angle γ depends on the problem to be solved. Flow fields showing mild variations of the surface elevation can be adequately represented by vertical motion of the nodes. For highly contorted flows the z'-axis may be given by the local velocity vector so that surface nodes tend to accumulate around locations experiencing large changes in boundary shape. For nodes in contact with solid

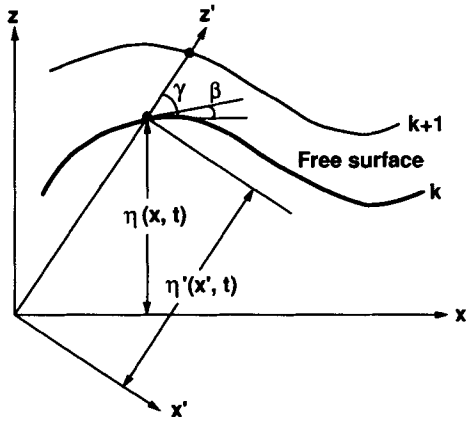

Figure 2. Movement of a surface node along the z'-axis

boundaries the angle γ is determined by the geometry of the wall so that the node remains attached to the boundary.

With the notation of Figure 2, equations (11) and (12) respectively become

$$\frac{\partial \eta'}{\partial t} = \frac{1}{\sin(\gamma-\beta)} \frac{\partial \Phi}{\partial n} \quad \text{on } z' = \eta', \tag{14}$$

$$\left(\frac{\partial \Phi}{\partial t}\right)_{x'} = -\eta - \frac{1}{We^2}\frac{1}{R} - \frac{1}{2}\left[\left(\frac{\partial \Phi}{\partial s}\right)^2 - \frac{2}{\tan(\gamma-\beta)}\frac{\partial \Phi}{\partial n}\frac{\partial \Phi}{\partial s} - \left(\frac{\partial \Phi}{\partial n}\right)^2\right], \tag{15}$$

where the subscript on the time derivative indicates that x' is to be held fixed.

3. THE BOUNDARY ELEMENT METHOD

The boundary value problem described in the previous section can be transformed by means of Green's second identity into an integral equation as shown by Liggett and Liu:[2]

$$\alpha\Phi(\mathrm{P}) = \int_\Gamma \left(\Phi(\mathrm{Q})\frac{\partial(\ln r)}{\partial n} - \ln r \frac{\partial \Phi(\mathrm{Q})}{\partial n}\right) \mathrm{d}s, \tag{16}$$

where Γ is the boundary of the flow region and r is the distance from point P to a point Q located on the boundary. Point P can be either in the interior of the domain or on the boundary. In the former case $\alpha = 2\pi$, whereas in the latter α is the angle subtended by the boundary at a point P. Equation (16) yields the value of the potential at P provided that both the potential and its normal derivative are known on the boundary.

Equation (16) is an integral equation for the potential or the normal derivative when P is moved to the boundary. A set of points connected by straight lines is used to approximate the boundary of the flow region; linear shape functions are used to represent the variation of the flow variables along the elements. Additional details of the implementation are discussed in Liggett and Liu.[2]

Following Liggett,[1] once the boundary is discretized, the integral equation (16) applied to a base point i located on the boundary results in

$$\alpha_i^k \Phi_i^k = \sum_{j=1}^{N_\mathrm{E}} \left[\Phi_j^k T_j^\mathrm{a} + \Phi_{j+1}^k T_j^\mathrm{b} + \left(\frac{\partial \Phi}{\partial n}\right)_j^k T_j^\mathrm{c} + \left(\frac{\partial \Phi}{\partial n}\right)_{j+1}^k T_j^\mathrm{d}\right], \tag{17}$$

where N_E is the number of elements on the boundary of the flow region and

$$T^\mathrm{a} = -I_1^\xi + I_1 \xi_{j+1}, \tag{18}$$

$$T^\mathrm{b} = I_1^\xi - I_1 \xi_j, \tag{19}$$

$$T^\mathrm{c} = -I_2^\xi + I_2 \xi_{j+1}, \tag{20}$$

$$T^\mathrm{d} = I_2^\xi - I_2 \xi_j, \tag{21}$$

with

$$I_1^\xi = \int_{\xi_j}^{\xi_{j+1}} -\frac{\xi\zeta_i}{r}\,\mathrm{d}A, \tag{22}$$

$$I_1 = \int_{\xi_j}^{\xi_{j+1}} -\frac{\zeta_i}{r^2}\,\mathrm{d}A, \tag{23}$$

$$I_2^{\xi} = \int_{\xi_j}^{\xi_{j+1}} \xi \ln r \, dA, \tag{24}$$

$$I_2 = \int_{\xi_j}^{\xi_{j+1}} \ln r \, dA. \tag{25}$$

Figure 3 describes the geometric parameters which appear in the integrals. All of the integrals can be computed analytically and the final expressions for equations (18)–(21) appear in Appendix I.

Setting $\partial\Phi/\partial n = 0$ on all parts of the boundary results in a constant potential everywhere. Introducing this fact in equation (17) yields the result that α_i is equal to the sum of T^a and T^b for all the elements.

4. COMPUTATIONAL STRATEGY

A straightforward procedure often used to calculate the position of the free surface at all times is the mixed Eulerian–Lagrangian method.[3] If N nodes are used to discretize the solid boundaries and M nodes are used to represent the free surface, there are $N+M$ unknown potentials and M unknown normal derivatives. Application of equation (17) yields $N+M$ boundary element equations; M additional equations are obtained from the dynamic boundary condition (12) once it has been properly linearized and written in finite difference form. A matrix equation for this system can be written as

$$[R]\{\Phi\} = [L]\left\{\frac{\partial\Phi}{\partial n}\right\}, \tag{26}$$

where $[R]$ and $[L]$ are functions of the geometry and the shape functions and the vectors $\{\Phi\}$ and $\{\partial\Phi/\partial n\}$ contain the nodal values of the flow variables. The equations can be assembled in a linear system that is solved for the $N+2M$ unknown flow variables. The kinematic boundary condition is then applied to move the M nodes on the free surface in a Lagrangian fashion to their new positions. The procedure is repeated for subsequent time steps. Variations on this process were used by Kim *et al.*[4] who applied the method to investigate the run-up of solitary waves, and by Nakayama and Washizu[5] to study non-linear sloshing in closed two-dimensional containers.

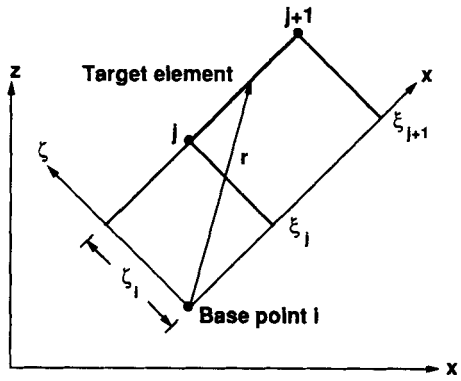

Figure 3. Local co-ordinate system to integrate over one linear element between nodes j and $j+1$. Point i is the base point

5. A GEOMETRICAL INCONSISTENCY

If the algorithm outlined above is followed, an obvious inconsistency results because the governing equation (26) is solved in an Eulerian frame of reference. Therefore the matrices R and L are evaluated in terms of the geometry of the flow domain at the old time step. Denoting the time level with a superscript, equation (26) is

$$[R]^k\{\Phi\}^{k+1}=[L]^k\left\{\frac{\partial\Phi}{\partial n}\right\}^{k+1}. \tag{27}$$

This inconsistency was pointed out by Liggett[1] in applying the BEM to free surface groundwater flow. The appearance of the geometry and the flow variables at different time levels in (27) results in a non-linearity which is not immediately apparent but is illustrated subsequently.

One way to circumvent the problem of enforcing the boundary conditions at an unknown location is to take equation (27) as a linearization of the actual equations and to use the most recently computed geometric variables as a guess for their values at the next time level. Then, after updating the geometry to level $k+1$, the flow variables are recalculated to check the adequacy of the guess. The process can be repeated iteratively until the guessed and computed values agree.

Another approach used by several authors to treat the non-linearity is to use a series expansion of the governing equations. Dold and Peregrine[6] employed the complex variable BEM combined with higher expansions of the differential equations. Dommermuth and Yue[7] extended the method to the axisymmetric case. A different technique was used by Liggett[1] who proposed a series expansion of the integral equation and the boundary conditions so that equation (26) can be written in a fully consistent manner, namely

$$[R]^{k+1}\{\Phi\}^{k+1}=[L]^{k+1}\left\{\frac{\partial\Phi}{\partial n}\right\}^{k+1}. \tag{28}$$

The development of this expression was presented by Liggett for the case of free surface groundwater flow for which the dynamic boundary condition reduces to a rather simple form. One objective of the present paper is to derive the detailed terms of equation (28) for the case of the hydrodynamic problem.

6. DERIVATION OF A CONSISTENT FORMULATION

In this section an expansion of the governing equations is carried out. The expansion leads to a set of consistent, linearized equations for hydrodynamic free surface problems. Additional details are available in Reference 8.

6.1. Expansion of the integral equation

Equation (17) can be rewritten for the advanced time step as

$$\begin{aligned}(\alpha_i^k+\Delta\alpha_i)(\Phi_i^k+\Delta\Phi_i)=\sum_{j=1}^{N_E}\Big\{&(\Phi_j^k+\Delta\Phi_j)(T_j^a+\Delta T_j^a)+(\Phi_{j+1}^k+\Delta\Phi_{j+1})(T_j^b+\Delta T_j^b)\\&+\left[\left(\frac{\partial\Phi}{\partial n}\right)_j^k+\Delta\left(\frac{\partial\Phi}{\partial n}\right)_j\right](T_j^c+\Delta T_j^c)+\left[\left(\frac{\partial\Phi}{\partial n}\right)_{j+1}^k+\Delta\left(\frac{\partial\Phi}{\partial n}\right)_{j+1}\right](T_j^d+\Delta T_j^d)\Big\},\end{aligned} \tag{29}$$

where the incremental Δ-terms reflect the change in the geometry and the flow variables with respect to the previous time level. The ΔT and $\Delta\alpha$-terms in (29) reflect the non-linearity stemming

from applying the boundary conditions at the unknown position of the free surface. The procedure of applying the boundary conditions at the known time level is equivalent to linearizing the equations assuming that the ΔT and $\Delta\alpha$-terms are zero.

Subtracting (17) from (29) and neglecting the second-order terms produces

$$\alpha_i^k\Delta\Phi_i+\Phi_i^k\Delta\alpha_i=\sum_{j=1}^{N_E}\left[\Phi_j^k\Delta T_j^a+T_j^a\Delta\Phi_j+\Phi_{j+1}^k\Delta T_j^b+T_j^b\Delta\Phi_{j+1}\right.$$
$$\left.+\left(\frac{\partial\Phi}{\partial n}\right)_j^k\Delta T_j^c+T_j^c\Delta\left(\frac{\partial\Phi}{\partial n}\right)_j+\left(\frac{\partial\Phi}{\partial n}\right)_{j+1}^k\Delta T_j^d+T_j^d\Delta\left(\frac{\partial\Phi}{\partial n}\right)_{j+1}\right], \tag{30}$$

where the Δ-quantities appear as unknowns.

The change in the geometry, expressed by ΔT and $\Delta\alpha$, is found from the integration from base point i over the element subtended by nodes j and $j+1$ (see Figure 3) as a function of the co-ordinates of these three points. In terms of the x- and z-coordinates,

$$\Delta T=\frac{\partial T}{\partial x_i}\Delta x_i+\frac{\partial T}{\partial x_j}\Delta x_j+\frac{\partial T}{\partial x_{j+1}}\Delta x_{j+1}+\frac{\partial T}{\partial z_i}\Delta z_i+\frac{\partial T}{\partial z_j}\Delta z_j+\frac{\partial T}{\partial z_{j+1}}\Delta z_{j+1}, \tag{31}$$

where T is either T^a, T^b, T^c or T^d. Further, the change in the global co-ordinates is determined from the changes in the local co-ordinate system over which the integrations in equations (22)–(25) are carried out; for example,

$$\frac{\partial T}{\partial x_j}=\frac{\partial T}{\partial\xi_j}\frac{\partial\xi_j}{\partial x_j}+\frac{\partial T}{\partial\xi_{j+1}}\frac{\partial\xi_{j+1}}{\partial x_j}+\frac{\partial T}{\partial\zeta_i}\frac{\partial\zeta_i}{\partial x_j}, \tag{32}$$

where the symbols correspond to the notation in Figure 3. As before, $\Delta\alpha_i$ can be determined as the sum of ΔT^a and ΔT^b over all the elements on the boundary.

Summarizing, the required derivatives in (31) and (32) are

$$\frac{\partial(T^a,T^b,T^c,T^d)}{\partial(\xi_j,\xi_{j+1},\zeta_i)},\qquad\frac{\partial(\xi_j,\xi_{j+1},\zeta_i)}{\partial(x_j,x_{j+1},x_i,z_j,z_{j+1},z_i)}. \tag{33}$$

These derivatives can be found by differentiating the expressions given in Appendix I. From Figure 2, Δx and Δz are related to $\Delta\eta'$ by

$$\Delta x=\Delta\eta'\cos\gamma,\qquad\Delta z=\Delta\eta'\sin\gamma. \tag{34}$$

The final form of the boundary element equation is

$$\alpha_i^k\Delta\Phi_i-\sum_{j=1}^{N_E}\left[T_j^a\Delta\Phi_j+T_j^b\Delta\Phi_{j+1}+T_j^c\Delta\left(\frac{\partial\Phi}{\partial n}\right)_j+T_j^d\Delta\left(\frac{\partial\Phi}{\partial n}\right)_{j+1}\right]$$
$$=-\Phi_i^k\Delta\alpha_i+\sum_{j=1}^{N_E}\left[\Phi_j^k\Delta T_j^a+\Phi_{j+1}^k\Delta T_j^b+\left(\frac{\partial\Phi}{\partial n}\right)_j^k\Delta T_j^c+\left(\frac{\partial\Phi}{\partial n}\right)_{j+1}^k\Delta T_j^d\right], \tag{35}$$

where

$$\Delta T=\Delta\eta_i'\delta_i T+\Delta\eta_j'\delta_j T+\Delta\eta_{j+1}'\delta_{j+1}T, \tag{36}$$

$$\delta_i=\cos\gamma_i\frac{\partial}{\partial x_i}+\sin\gamma_i\frac{\partial}{\partial z_i}, \tag{37}$$

$$\frac{\partial}{\partial x_i}=\frac{\partial\xi_j}{\partial x_i}\frac{\partial}{\partial\xi_j}+\frac{\partial\xi_{j+1}}{\partial x_i}\frac{\partial}{\partial\xi_{j+1}}+\frac{\partial\zeta_i}{\partial x_i}\frac{\partial}{\partial\zeta_i}. \tag{38}$$

Equation (35), with the definitions (36)–(38), provides N_E equations relating $\Delta\Phi$, $\Delta(\partial\Phi/\partial n)$, and $\Delta\eta'$. For linear boundary elements, $N_E = N + M$, where N_E is the number of elements and N and M are the numbers of nodes on the solid boundary and free surface respectively.

6.2. Expansion of the free surface dynamic boundary condition

The dynamic boundary condition in (15) can be used to expand the potential to the advanced time level:

$$\Delta\Phi = \Delta t[\, Y^k + \theta_1 \Delta Y], \tag{39}$$

where

$$\Delta\Phi = \Phi^{k+1} - \Phi^k, \tag{40a}$$

$$\Delta Y = Y^{k+1} - Y^k \tag{40b}$$

and

$$Y^k = -\eta^k - \frac{1}{We^2}\frac{1}{R^k} - \frac{1}{2}\left[\left(\frac{\partial\Phi}{\partial s}\right)^2 - \frac{2}{\tan(\gamma-\beta)}\frac{\partial\Phi}{\partial n}\frac{\partial\Phi}{\partial s} - \left(\frac{\partial\Phi}{\partial n}\right)^2\right]^k. \tag{41}$$

The parameter θ_1 acts as an implicitness factor in the time-stepping scheme. Further expansion of Y^k leads to

$$\begin{aligned}\Delta Y = &-\Delta\eta - \frac{\theta_2}{\theta_1}\frac{1}{We^2}\Delta R^{-1} - \left(\frac{\partial\Phi}{\partial s}\right)^k \Delta\left(\frac{\partial\Phi}{\partial s}\right) + \left(\frac{\partial\Phi}{\partial n}\right)^k \Delta\left(\frac{\partial\Phi}{\partial n}\right)\\ &+ \frac{1}{\tan(\gamma-\beta^k)}\left[\left(\frac{\partial\Phi}{\partial n}\right)^k \Delta\left(\frac{\partial\Phi}{\partial s}\right) + \left(\frac{\partial\Phi}{\partial s}\right)^k \Delta\left(\frac{\partial\Phi}{\partial n}\right)\right]\\ &- \frac{\sec^2\gamma}{(\tan\gamma - \tan\beta^k)^2}\left(\frac{\partial\Phi}{\partial s}\right)^k \left(\frac{\partial\Phi}{\partial n}\right)^k \Delta\tan\beta,\end{aligned} \tag{42}$$

where θ_2 is a second implicitness factor. The tangential derivative of the potential is approximated by a three-point formula so that

$$\Delta\left(\frac{\partial\Phi}{\partial s}\right)_j = C_j^+ \Delta\Phi_{j+1} + C_j^0 \Delta\Phi_j + C_j^- \Delta\Phi_{j-1}. \tag{43}$$

The coefficients of $\Delta\Phi$ in (43) depend on the co-ordinates of the free surface nodes:

$$C_j^+ = \frac{I_{j-1}^2}{I_j I_{j-1}^2 + I_{j-1} I_j^2}, \qquad C_j^0 = \frac{I_{j+1}^2 - I_{j-1}^2}{I_j I_{j-1}^2 + I_{j-1} I_j^2}, \qquad C_j^- = -\frac{I_{j+1}^2}{I_j I_{j-1}^2 + I_{j-1} I_j^2}, \tag{44}$$

where I_j is the distance between nodes 1 and j measured along the free surface.

The terms ΔR^{-1} and $\Delta\tan\beta$ are derived from the geometry of the free surface. For this purpose a parabola is fitted choosing three contiguous nodes and the resulting expression is used to determine the slope and curvature at the middle point. After some manipulation, $\Delta\tan\beta$ and ΔR^{-1} are given by

$$\Delta\tan\beta_j = B_j^- \Delta\eta'_{j-1} + B_j^0 \Delta\eta'_j + B_j^+ \Delta\eta'_{j+1}, \tag{45}$$

$$\Delta R_j^{-1} = A_j^- \Delta\eta'_{j-1} + A_j^0 \Delta\eta'_j + A_j^+ \Delta\eta'_{j+1}. \tag{46}$$

The coefficients multiplying the $\Delta\eta'$-terms and the procedure to obtain equations (45) and (46) appear in Appendix II.

The final form of the dynamic boundary condition is

$$D_0 = D_1\Delta\Phi_{j+1} + D_2\Delta\Phi_j + D_3\Delta\Phi_{j-1} + D_4\,\Delta\left(\frac{\partial\Phi}{\partial n}\right)_j + D_5\Delta\eta'_{j-1} + D_6\Delta\eta'_j + D_7\Delta\eta'_{j+1}, \tag{47}$$

where

$$D_0 = -\Delta t\left\{-\eta - \frac{1}{2}\left[\left(\frac{\partial\Phi}{\partial s}\right)_j^2 + \left(\frac{\partial\Phi}{\partial n}\right)_j^2\right] - \left[\cot(\gamma_j-\beta_j)\left(\frac{\partial\Phi}{\partial s}\right)_j^2\left(\frac{\partial\Phi}{\partial n}\right)_j^2\right] - \frac{1}{We^2}R^{-1}\right\}^k, \tag{48}$$

$$D_1 = \Delta t\, C_j^+\,\theta_1\left[\cot(\gamma_j-\beta_j)\left(\frac{\partial\Phi}{\partial n}\right)_j - \left(\frac{\partial\Phi}{\partial s}\right)_j\right]^k, \tag{49}$$

$$D_2 = \Delta t\, C_j^0\,\theta_1\left[\cot(\gamma_j-\beta_j)\left(\frac{\partial\Phi}{\partial n}\right)_j - \left(\frac{\partial\Phi}{\partial s}\right)_j\right]^k - 1, \tag{50}$$

$$D_3 = \Delta t\, C_j^-\,\theta_1\left[\cot(\gamma_j-\beta_j)\left(\frac{\partial\Phi}{\partial n}\right)_j - \left(\frac{\partial\Phi}{\partial s}\right)_j\right]^k, \tag{51}$$

$$D_4 = \Delta t\,\theta_1\left[\cot(\gamma_j-\beta_j)\left(\frac{\partial\Phi}{\partial s}\right)_j + \left(\frac{\partial\Phi}{\partial n}\right)_j\right]^k, \tag{52}$$

$$D_5 = \Delta t\, B_j^+\,\theta_1\left[\left(\frac{\partial\Phi}{\partial n}\right)_j\left(\frac{\partial\Phi}{\partial s}\right)_j\frac{\sec^2\gamma_j}{(\tan\gamma_j-\tan\beta_j)^2}\right]^k - \Delta t\,\theta_2\,\frac{A_j^+}{We^2}, \tag{53}$$

$$D_6 = \Delta t\, B_j^0\,\theta_1\left[\left(\frac{\partial\Phi}{\partial n}\right)_j\left(\frac{\partial\Phi}{\partial s}\right)_j\frac{\sec^2\gamma_j}{(\tan\gamma_j-\tan\beta_j)^2}\right]^k - \Delta t\,\theta_2\left(\frac{A_j^0}{We^2} + \sin\gamma_j\right), \tag{54}$$

$$D_7 = \Delta t\, B_j^-\,\theta_1\left[\left(\frac{\partial\Phi}{\partial n}\right)_j\left(\frac{\partial\Phi}{\partial s}\right)_j\frac{\sec^2\gamma_j}{(\tan\gamma_j-\tan\beta_j)^2}\right]^k - \Delta t\,\theta_2\,\frac{A_j^-}{We^2}. \tag{55}$$

6.3. *Expansion of the free surface kinematic boundary condition*

The kinematic boundary condition in (14) is discretized as

$$\Delta\eta = \Delta t[Z^k + \theta_3\Delta Z], \tag{56}$$

where

$$\Delta\eta' = (\eta')^{k+1} - (\eta')^k, \tag{57a}$$

$$\Delta Z = Z^{k+1} - Z^k \tag{57b}$$

and

$$Z^k = \frac{1}{\sin(\gamma-\beta^k)}\left(\frac{\partial\Phi}{\partial n}\right)^k. \tag{58}$$

The parameter θ_3 acts as an implicitness factor similar to θ_1 and θ_2 in the dynamic boundary condition. Expansion of Z^k leads to

$$\Delta Z = \frac{1}{\sin(\gamma-\beta^k)}\left(\frac{\partial\Phi}{\partial n}\right)^k + \frac{\theta_3}{\sin(\gamma-\beta^k)}\,\Delta\left(\frac{\partial\Phi}{\partial n}\right) + \frac{\theta_3}{\sin^2(\gamma-\beta^k)}\left(\frac{\partial\Phi}{\partial n}\right)^k\cos^3\beta^k(\cos\gamma + \sin\gamma\tan\beta^k)\,\Delta\tan\beta. \tag{59}$$

Proceeding in the same way as with the dynamic boundary condition, the final discretization of the kinematic condition is

$$E_0 = E_1 \Delta\left(\frac{\partial\Phi}{\partial n}\right) + E_2 \Delta\eta'_{j+1} + E_3 \Delta\eta'_j + E_4 \Delta\eta'_{j-1}, \tag{60}$$

where

$$E_0 = -\Delta t\left[\frac{1}{\sin(\gamma_j - \beta_j)}\left(\frac{\partial\Phi}{\partial n}\right)_j\right]^k, \tag{61}$$

$$E_1 = \frac{\Delta t\theta_3}{\sin(\gamma_j - \beta_j^k)}, \tag{62}$$

$$E_2 = \Delta t\theta_3 B_j^+\left[\frac{\cos^3\beta_j(\cos\gamma_j + \sin\gamma_j\tan\beta_j)}{\sin^2(\gamma_j - \beta_j)}\left(\frac{\partial\Phi}{\partial n}\right)_j\right]^k, \tag{63}$$

$$E_3 = \Delta t\theta_3 B_j^0\left[\frac{\cos^3\beta_j(\cos\gamma_j + \sin\gamma_j\tan\beta_j)}{\sin^2(\gamma_j - \beta_j)}\left(\frac{\partial\Phi}{\partial n}\right)_j\right]^k - 1, \tag{64}$$

$$E_4 = \Delta t\theta_3 B_j^-\left[\frac{\cos^3\beta_j(\cos\gamma_j + \sin\gamma_j\tan\beta_j)}{\sin^2(\gamma_j - \beta_j)}\left(\frac{\partial\Phi}{\partial n}\right)_j\right]^k. \tag{65}$$

6.4. Assembly of the equations

The governing equations consist of the boundary element equation (35) and the dynamic and kinematic free surface boundary conditions given respectively by (47) and (60). The governing equations, including the free surface boundary conditions, are all linear in the corrections to the potential, the normal derivatives and the position of the nodes on the free surface (i.e. linear in $\Delta\Phi$, $\Delta(\partial\Phi/\partial n)$ and $\Delta\eta'$). Thus a system of linear algebraic equations results for the unknown flow variables on the boundary and the location of the free surface at the advanced time step.

The system of equations has a dimension of $N + 3M$, where N and M are the numbers of nodes on the solid boundaries and free surface respectively.

7. EXAMPLES

The consistent method outlined in the previous section was implemented in a computer code. To verify its performance, computed results were compared against physical experiments, existing non-linear analytical solutions and numerical results obtained with an iterative Eulerian–Lagrangian scheme. In the comparisons the Weber number was either infinite or sufficiently large so that surface tension effects could be neglected. Unless otherwise noted, the surface nodes were moved with the local velocity vector and the implicitness parameters $\theta_1, \theta_2, \theta_3$ were set to a common value given by $\theta = 0{\cdot}55$. This section summarizes the results of the comparisons.

7.1. Triangular wave

Figure 4 shows the initial position of a free surface in a container. The subsequent motion of the fluid is due to gravitational forces. The problem allows a comparison of the two numerical methods for a moderate-amplitude wave.

The discretization of the geometry was the same for both methods, i.e. 42 nodes with 25 on the free surface. To establish a common set of parameters, no attempt was made to use a dynamically

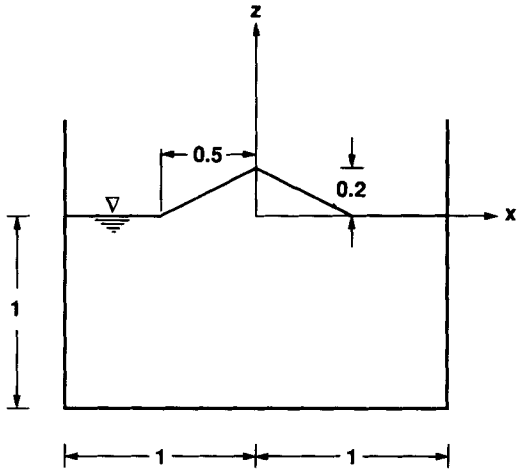

Figure 4. A triangular wave in a container

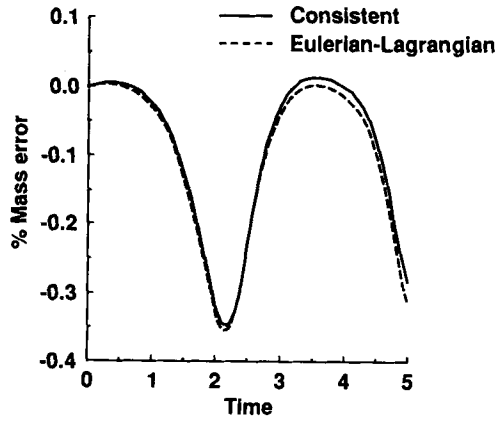

Figure 5. Evolution in time of the mass error for the triangular wave using two computational schemes. Approximately equal mass errors result using a time step four times larger for the consistent scheme

varying time step. The iterative Eulerian–Lagrangian scheme[3] used 0·005 as a time step, which is such that no more than one iteration was needed at each time level to achieve convergence. The time step for the consistent scheme was set to 0·02, which produces a mass error similar to that obtained with the iterative scheme.

The percentage mass error for the two methods is shown in Figure 5. The mass error is computed as the difference between the mass at a particular time level and the initial mass, divided by the initial mass. From Figure 5 it is apparent that the consistent scheme, even though it uses a four-times-larger time step, yields a mass error which is comparable to, but slightly less than, that obtained with the iterative scheme. Figure 6, which displays the time history of the elevation of two points on the free surface, shows that the results are practically identical for the two schemes.

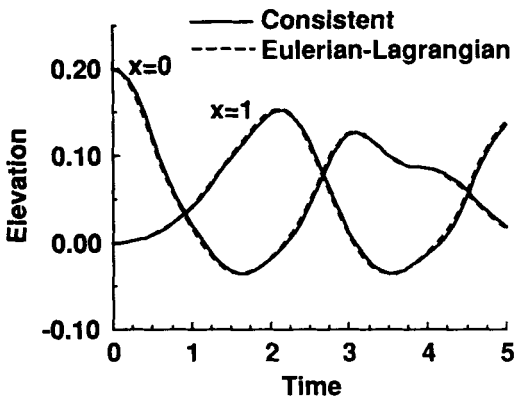

Figure 6. Elevation of the centre and right-most points in the triangular wave using two computational schemes

Owing to the additional computations and the larger linear system, the consistent scheme requires more computer resources per time step. However, the overall computing time is reduced by choosing a larger time increment. On a VAX 3600 the iterative scheme took 5074 CPU seconds to simulate 5 s of wave motion. The same calculation using the consistent scheme employed 1642 CPU seconds. Therefore, although each time step took approximately 30% longer with the consistent scheme, the overall speed-up factor was 3·1.

7.2. Generation of tsunamis

A laboratory physical model for the generation and propagation of large ocean waves produced by sea bed movements was developed by Hammack.[9] The physical model employed a channel similar to the one depicted in Figure 7. Results from the experimental model are compared in Figure 8 with the predictions of the present consistent BEM.

In the laboratory experiments a piston on the bottom moved upwards in time such that

$$\frac{\partial \Phi}{\partial n} = -\alpha_0 d_0 e^{-\alpha_0 t}. \tag{66}$$

By varying the velocity of the piston, three cases are discussed by Hammack: impulsive, transitional and creeping. The values of the parameters α_0 and d_0 for the three cases are $\alpha_0 = 5{\cdot}843$, $1{\cdot}041$, $0{\cdot}046$ and $d_0 = 0{\cdot}010$, $0{\cdot}005$, $0{\cdot}015$ respectively. All variables are dimensionless.

For the boundary element calculations the domain was limited to two units in the horizontal direction as shown in Figure 7. Equation (66) was used as a boundary condition for the region of the piston. In the absence of an appropriate radiation boundary condition at the right wall, reflected waves will be generated and move towards the left. The discretization employed 72 nodes with 43 on the free surface. Figure 8 shows the time history of the left-most surface node compared with the experiments. The computed solutions (solid lines) agree well with the experimental data up to the point when reflected waves reach the left wall. The maximum wave amplitudes in Figure 8 are $0{\cdot}2$ and $0{\cdot}1$ of the layer depth in the impulsive and transitional cases respectively and, according to Hammack,[9] the experiments show significant non-linear effects.

7.3. Solitary wave

To assess the performance of the consistent scheme against an analytical solution, a propagating solitary wave in a tank was examined. The wave was initially set moving to the right as shown in Figure 9 and the surface profiles were followed in time.

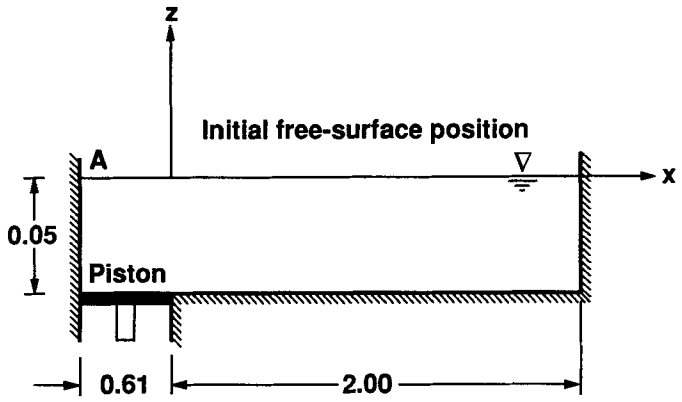

Figure 7. Water tank to simulate waves generated by bottom movement

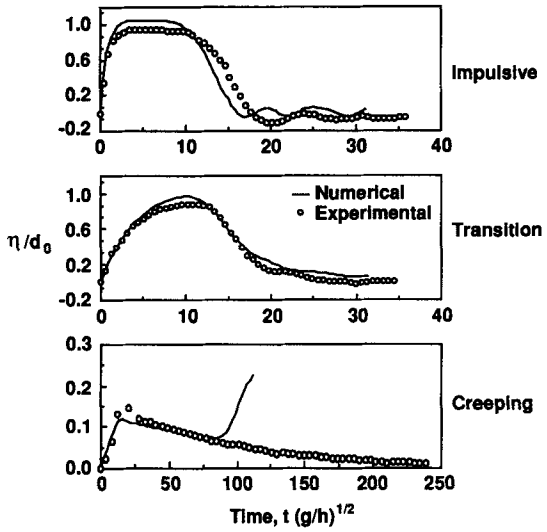

Figure 8. Movement of the surface node at the left wall ($x=-0{\cdot}61$) for the three cases in Hammack[9]

The solitary wave is an approximate analytical solution in which weakly non-linear effects balance dispersive effects so that the wave maintains its original shape as it moves.[10,11] Figure 9 shows the computational domain for the test problem. Using the fluid depth as the reference length to obtain dimensionless variables, the solitary wave is generated by establishing the following initial conditions on the free surface:

$$\Phi(x,0)=\frac{1}{\lambda}\left(1-\tfrac{1}{4}H+\tfrac{1}{3}H\tanh^2\mu\right)\tanh\mu\sqrt{\left(\frac{4}{3}\frac{H}{1-\frac{5}{4}H}\right)}+\frac{1}{\lambda}\operatorname{sech}^2\mu\tanh\mu\sqrt{[\tfrac{3}{4}H^3(1-\tfrac{5}{4}H)]}, \tag{67}$$

$$\eta(x,0)=H(1-\tfrac{3}{4}H\tanh^2\mu)\operatorname{sech}^2\mu, \tag{68}$$

where

$$\mu(x,0)=(x-x_0)\sqrt{[\tfrac{3}{4}H(1-\tfrac{5}{4}H)]}, \tag{69a}$$

$$\lambda=1+\tfrac{1}{2}H-\tfrac{3}{20}H^2. \tag{69b}$$

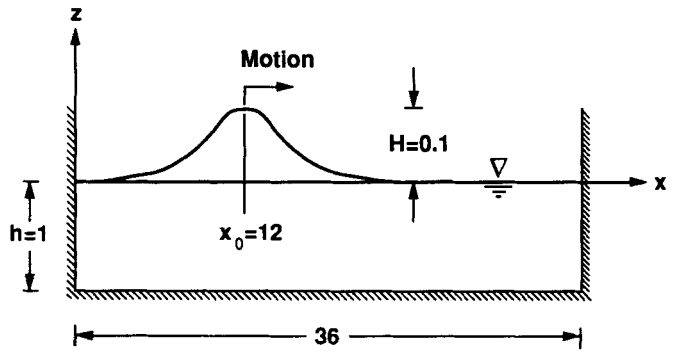

Figure 9. Initial condition and computational domain for the solitary wave

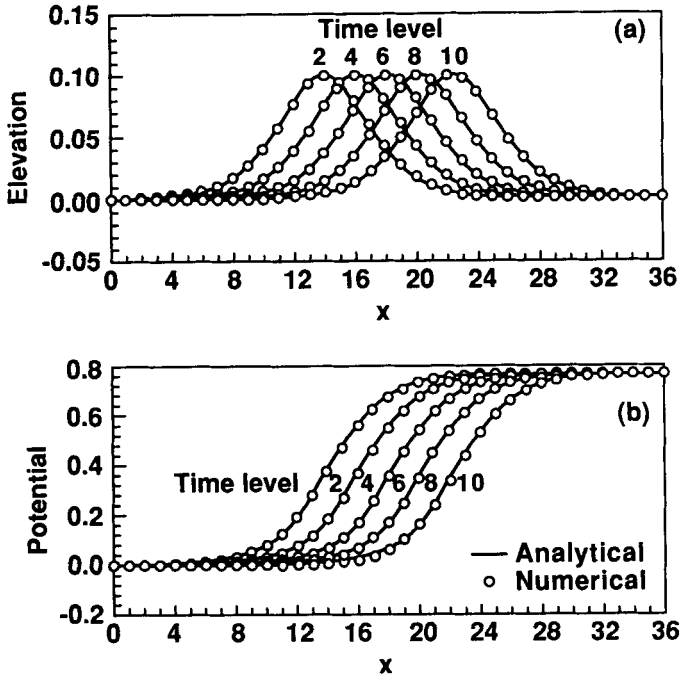

Figure 10. Motion of the solitary wave compared with the analytical solution

The foregoing is a second-order-correct analytical solution;[11] x_0 corresponds to the initial location of the crest (taken to be 12) and λ is the wave speed.

Figure 10 shows the motion of a calculated wave compared to the analytical solution. The latter is simply the initial profile displaced in time. The free surface height and the velocity potential are shown and the agreement for both is excellent. The numerical solution employed $\Delta t = 0{\cdot}25$, $\Delta s = 0{\cdot}125$ and $\theta = 0{\cdot}5$, which corresponds to a fine-mesh solution. Surface nodes were moved vertically and only every eighth node is displayed. To achieve the agreement shown it was necessary to use the second-order analytical solution as opposed to a simpler first-order solution. A discussion of the effect of truncation errors on the numerical solution is given in Section 8.

7.4. Non-linear standing waves

Free oscillations of moderate-amplitude non-linear waves are examined in the domain shown in Figure 11 and are compared against a higher-order analytical solution. For the case of infinite depth an approximate analytical solution was found by Penney and Price[12] in terms of a fifth-order perturbation expansion. According to the theory, the assumption of deep water is valid in a container with the dimensions shown in the figure.

The initial location of the surface is given by

$$\eta(x,0)=(\varepsilon+\tfrac{1}{32}\varepsilon^3-\tfrac{47}{1344}\varepsilon^5)\cos x+(\tfrac{1}{2}\varepsilon^2-\tfrac{79}{672}\varepsilon^4)\cos 2x$$
$$+(\tfrac{3}{8}\varepsilon^3-\tfrac{125563}{591136}\varepsilon^5)\cos 3x+\tfrac{1}{3}\varepsilon^4\cos 4x+\tfrac{295}{768}\varepsilon^5\cos 5x, \tag{70}$$

where ε is a measure of the amplitude and is related to the frequency by

$$\omega^2=1-\tfrac{1}{4}\varepsilon^2-\tfrac{13}{128}\varepsilon^4. \tag{71}$$

The frequency ω is equal to $2\pi/\tau$, where τ is the dimensionless period. At the position given by equation (70) the surface is momentarily at rest and the potential is everywhere equal to zero on the surface.

The consistent boundary element calculation used 21 nodes on the free surface. Figure 12 shows the time history of two points on the surface for a 1/2-subharmonic wave with period $\tau=6{\cdot}32$. Two profiles of the surface are shown in Figure 13 at times $\tau/2$ and τ. From the figures it can be observed that the height of the crests is greater than the depth of the troughs, a well-known feature of non-linear waves. The computation agrees well with the approximate analytical solution.

8. TRUNCATION ERRORS

The leading truncation errors of the consistent BEM generally arise from the dynamic boundary condition. The error analysis is summarized in Appendix III. The form of the leading errors and their impact on the propagating solitary wave of Section 7.3 are discussed in this section.

A discrete solution of the dynamic boundary condition given by equation (15), when truncation errors are considered, corresponds to a solution of a modified form of the equation which is found

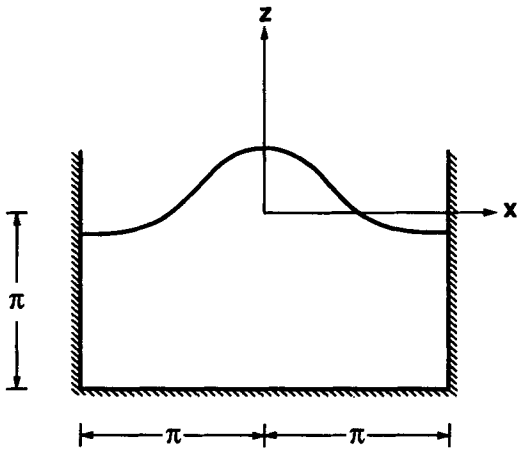

Figure 11. Flow domain for non-linear standing waves in a deep container

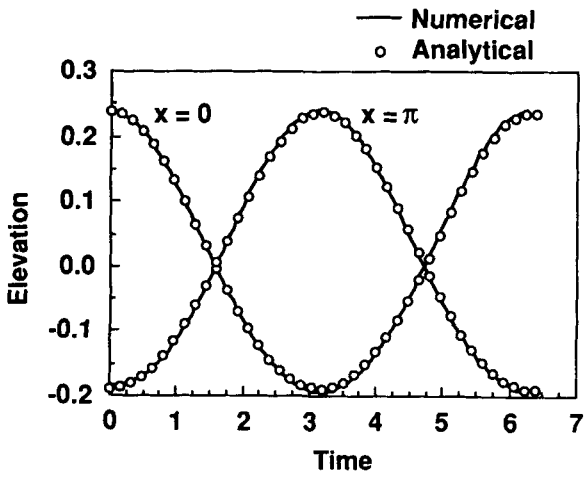

Figure 12. Time histories of two points on the free surface at $x=0$ and π for the non-linear standing wave in Figure 11

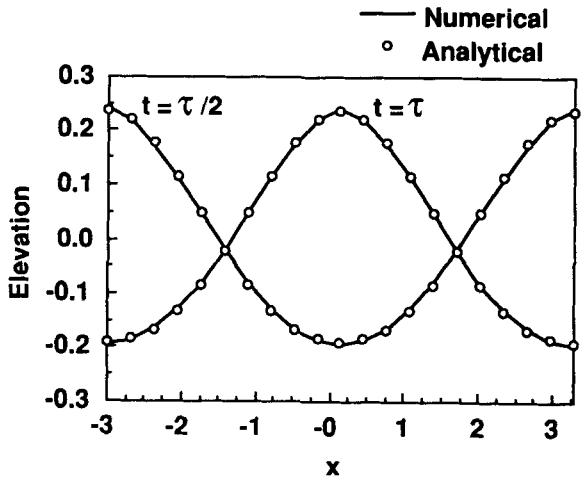

Figure 13. Surface profiles for non-linear standing waves corresponding to time levels of $\tau/2$ and τ, where τ is the period

by adding the following terms to the right side of (15):

$$(\theta-\tfrac{1}{2})\Delta t\left(\frac{\partial\Phi}{\partial s}\right)^2\frac{\partial^2\Phi}{\partial s^2}+O(\Delta t^2)-\tfrac{1}{6}(\Delta s^k)^2\left\{1+\theta\left[\left(\frac{\Delta s^{k+1}}{\Delta s^k}\right)^2-1\right]\right\}\frac{\partial\Phi}{\partial s}\frac{\partial^3\Phi}{\partial s^3}+O(\Delta t^3,\Delta t\Delta s^2,\Delta s^3), \tag{72}$$

where θ is the implicitness factor θ_1. Only the derivatives appearing in the leading truncation terms are shown; they are evaluated at time level $k+\theta$ and spatial position j, where $0\leq\theta\leq 1$. The spatial mesh increments at time levels k and $k+1$ are denoted by Δs^k and Δs^{k+1} respectively. Usually their ratio is close to unity, thus simplifying the third term. The leading truncation errors in (72) are first-order in time and second-order in space.

The effect of the spatial truncation error on the propagating solitary wave of Section 7.3 is illustrated in Figure 14. The impact of a coarse surface mesh is shown in Figures 14(a) and 14(b). The surface mesh is $\Delta s = 2$ as compared to $\Delta s = 0{\cdot}125$ in Figure 10. The numerical solution clearly suffers from dispersion or a false numerical wave speed, the magnitude of which varies over the profiles. To minimize the effects of time truncation errors in Figure 14, a small time step, $\Delta t = 0{\cdot}5$, and $\theta = 0{\cdot}5$ were used. Also, Δs refers to the average surface mesh and, when varied, the surface, bottom and end boundaries were meshed in the proportion $2 : \frac{4}{3} : \frac{1}{3}$.

The results in Figure 14 are consistent with the leading $(\Delta s)^2$-error term in equation (72). First, dispersion in the Φ-profile is suggested by the presence of the derivative $\partial^3\Phi/\partial s^3$. Secondly, the crossover points between the numerical and analytical Φ-profiles approximately correspond to the zeros of $\partial^3\Phi/\partial s^3$ as found from the analytical solution. Thirdly, an integral measure of the error, as shown in Figure 14(c), is proportional to $(\Delta s)^2$. The integral error is defined as the integral of $|\Phi_N - \Phi_R|$ over the spatial region $0 \leq x \leq 36$ at time $t = 10$, where Φ_N is a numerical solution and Φ_R a reference solution. The integral error in Figure 14(c) does not go through the origin when referenced against the second-order analytical solution, but does when referenced against a fine-spatial-mesh numerical solution. This is not unexpected since the analytical solution is an approximate solution of the non-linear equations.

Figure 15 is similar to Figure 14 and illustrates the effect of the leading time truncation error in equation (72) on the propagating solitary wave. The time error introduces the group $(\theta - 0{\cdot}5)\Delta t$,

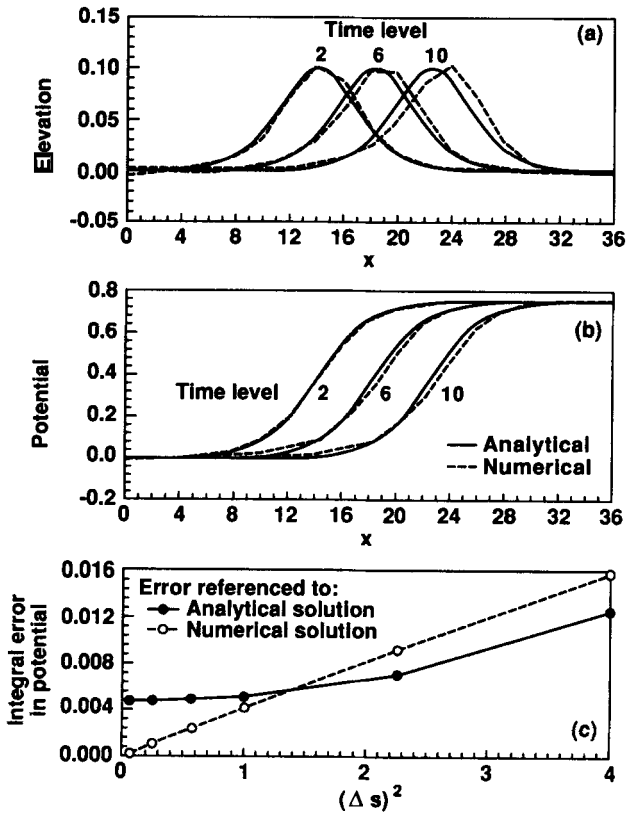

Figure 14. Effect of spatial truncation errors on the solitary wave

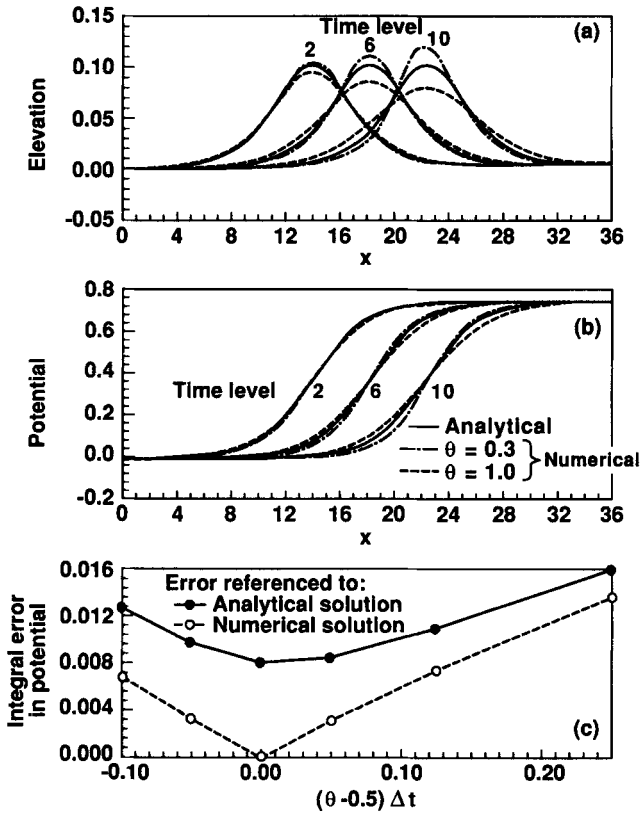

Figure 15. Effect of temporal truncation errors on the solitary wave

which changes sign when θ is above or below 0·5. To minimize the effect of spatial truncation errors on the results in Figure 15, a fairly fine spatial mesh of $\Delta s = 0{\cdot}5$ was used. The time step was $\Delta t = 0{\cdot}5$ in Figures 15(a) and 15(b) and was varied along with θ in Figure 15(c).

The time-evolving profiles in Figures 15(a) and 15(b) display the effect of the parameter θ. Positive and negative numerical damping appears when $\theta = 1$ and 0·3 respectively. With positive damping the wave decays in amplitude and the potential spreads out. With negative damping the wave grows in amplitude and the gradient of the potential steepens. Both effects are non-physical for the present problem, and the negative damping leads to unbounded growth of the wave amplitude.

The numerical damping is consistent with the leading time truncation term in (72), which contains $\partial^2\Phi/\partial s^2$. This is a damping term and its coefficient changes sign as noted to cause positive or negative damping. The leading time error is also consistent with the integral error in Figure 15(c), which is proportional to $(\theta - 0{\cdot}5)\Delta t$ when referenced against a fine-mesh numerical solution. The change of slope at $(\theta - 0{\cdot}5)\Delta t = 0$ is due to the use of absolute values in the integral error. Again, the integral error does not go to zero when referenced against the analytical solution. From a comparison of Figures 15(c) and 14(c), it appears that temporal truncation errors are often of similar magnitude to spatial truncation errors, but the temporal errors can be reduced by using θ-values close to 0·5.

The truncation error analysis was carried out in terms of the velocity potential Φ. Rather surprisingly, the form of the leading errors as given by (72) appears to apply to both the potential *and* the wave height profiles for the solitary wave. Furthermore, equation (72), representing the truncation errors in the dynamic boundary condition, appears to describe the leading errors in the entire numerical system.

9. CONCLUSIONS

A new boundary element algorithm has been developed to solve free surface, non-linear hydrodynamic problems under the assumption of potential flow. The formulation explicitly incorporates the non-linearity arising from the application of the free surface boundary conditions at an unknown location. The present scheme uses a series expansion of the geometric parameters and the flow variables appearing in the governing integral equation and free surface boundary conditions to obtain a more accurate estimate of the geometry at the new time level. The algebraic process is complex, but once the resulting expressions are implemented, the consistent method improves the computational speed for a given degree of accuracy. The method can be further improved by adding enhancements such as variability in the time step and condensation of the linear system.

ACKNOWLEDGEMENTS

The research reported in this paper was supported by a grant from the Xerox Corporation, Mechanical Engineering Sciences Laboratory, North Tarrytown, NY. Valuable discussions with Drs. Meng H. Lean and Palghat S. Ramesh of Xerox are gratefully acknowledged. Additional support was obtained from the National Science Foundation under grant ECE-8610119. Some of the computations employed the Cornell National Supercomputer Facility, a resource of the Theory Center at Cornell University, which is funded in part by the National Science Foundation, New York State, the IBM Corporation and other corporate sponsors.

APPENDIX I: GEOMETRIC COMPONENTS OF THE BOUNDARY ELEMENT EQUATION

Referring to Figure 3, the analytic expressions for equations (18)–(21) are

$$T^{a}=\frac{-\zeta_i}{2(\xi_{j+1}-\xi_j)}\ln\left(\frac{\zeta_i^2+\xi_{j+1}^2}{\zeta_i^2+\xi_j^2}\right)+\frac{\xi_{j+1}}{\xi_{j+1}-\xi_j}\left[\tan\left(\frac{\xi_{j+1}}{\zeta_i}\right)-\tan\left(\frac{\xi_j}{\zeta_i}\right)\right], \tag{73}$$

$$T^{b}=\frac{\zeta_i}{2(\xi_{j+1}-\xi_j)}\ln\left(\frac{\zeta_i^2+\xi_{j+1}^2}{\zeta_i^2+\xi_j^2}\right)-\frac{\xi_j}{\xi_{j+1}-\xi_j}\left[\tan\left(\frac{\xi_{j+1}}{\zeta_i}\right)-\tan\left(\frac{\xi_j}{\zeta_i}\right)\right], \tag{74}$$

$$\begin{aligned}T^{c}=&\frac{\zeta_i^2}{4(\xi_{j+1}-\xi_j)}\ln\left(\frac{\zeta_i^2+\xi_{j+1}^2}{\zeta_i^2+\xi_j^2}\right)-\xi_{j+1}\zeta_i\left[\tan\left(\frac{\xi_{j+1}}{\zeta_i}\right)-\tan\left(\frac{\xi_j}{\zeta_i}\right)\right]\\&+\frac{1}{4(\xi_{j+1}-\xi_j)}\{\xi_{j+1}^2[\ln(\zeta_i^2+\xi_{j+1}^2)-1]-\xi_j^2[\ln(\zeta_i^2+\xi_j^2)-1]\}\\&-\frac{\xi_{j+1}^2}{2(\xi_{j+1}-\xi_j)}\ln(\zeta_i^2+\xi_{j+1}^2)+\frac{\xi_{j+1}\xi_j}{2(\xi_{j+1}-\xi_j)}\ln(\zeta_i^2+\xi_j^2)+\xi_{j+1},\end{aligned} \tag{75}$$

$$T^{d}=\frac{-\zeta_i^2}{4(\xi_{j+1}-\xi_j)}\ln\left(\frac{\zeta_i^2+\xi_{j+1}^2}{\zeta_i^2+\xi_j^2}\right)+\xi_j\zeta_i\left[\tan\left(\frac{\xi_{j+1}}{\zeta_i}\right)-\tan\left(\frac{\xi_j}{\zeta_i}\right)\right]$$
$$-\frac{1}{4(\xi_{j+1}-\xi_j)}\{\xi_{j+1}^2[\ln(\zeta_i^2+\xi_{j+1}^2)-1]-\xi_j^2[\ln(\zeta_i^2+\xi_j^2)-1]\}$$
$$+\frac{\xi_{j+1}\xi_j}{2(\xi_{j+1}-\xi_j)}\ln(\zeta_i^2+\xi_{j+1}^2)-\frac{\xi_j^2}{2(\xi_{j+1}-\xi_j)}\ln(\zeta_i^2+\xi_j^2)-\xi_j. \tag{76}$$

The derivatives of these expressions with respect to the local co-ordinate system as given in the first part of equation (33) are obtained from the above formulae.

The transformation between global and local co-ordinate systems yields

$$\xi_{j+1}=\frac{(x_{j+1}-x_i)(x_{j+1}-x_j)+(z_{j+1}-z_i)(z_{j+1}-z_j)}{\sqrt{[(x_{j+1}-x_j)^2+(z_{j+1}-z_j)^2]}}, \tag{77}$$

$$\xi_j=\frac{(x_j-x_i)(x_{j+1}-x_j)+(z_j-z_i)(z_{j+1}-z_j)}{\sqrt{[(x_{j+1}-x_j)^2+(z_{j+1}-z_j)^2]}}, \tag{78}$$

$$\zeta_i=\frac{(z_j-z_i)(x_{j+1}-x_j)-(x_j-x_i)(z_{j+1}-z_j)}{\sqrt{[(x_{j+1}-x_j)^2+(z_{j+1}-z_j)^2]}}. \tag{79}$$

The derivatives in the second part of equation (33) are obtained from these equations.

APPENDIX II: SLOPES AND CURVATURES

Referring to Figure 16, a parabola is fitted through every three contiguous points on the free surface. The parabola is rotated so that its axis is normal to the line joining the two end points; therefore

$$p=z\sin\psi+x\cos\psi, \tag{80}$$

$$q=z\cos\psi-x\sin\psi, \tag{81}$$

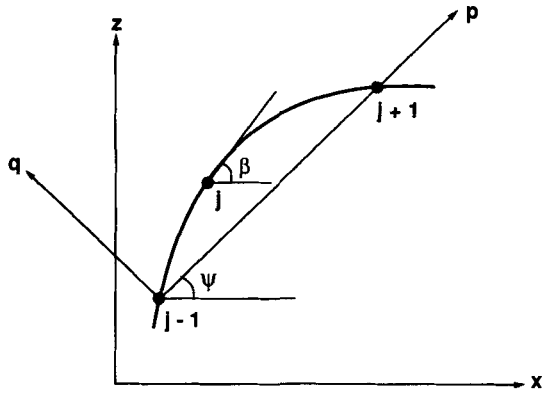

Figure 16. Three surface nodes fitted to a parabola

where

$$\tan\psi=\frac{z_{j+1}-z_{j-1}}{x_{j+1}-x_{j-1}}. \tag{82}$$

In this rotated system, if the equation for the parabola is

$$q=ap^2+bp+c, \tag{83}$$

the coefficients are given as

$$a=(1/D)[q_{j-1}(p_j-p_{j+1})-p_{j-1}(q_j-q_{j+1})+q_jp_{j+1}-q_{j+1}p_j], \tag{84}$$

$$b=(1/D)[p_{j-1}^2(q_j-q_{j+1})-q_{j-1}(p_j^2-p_{j+1}^2)+p_j^2q_{j+1}-p_{j+1}^2q_j], \tag{85}$$

$$c=(1/D)[p_{j-1}^2(q_{j+1}p_j-q_jp_{j+1})-p_j(p_j^2q_{j+1}-p_{j+1}^2q_j)+q_{j-1}(p_j^2p_{j+1}-p_{j+1}^2p_j)], \tag{86}$$

$$D=p_j^2(p_j-p_{j-1})-p_{j-1}(p_j^2-p_{j+1}^2)+p_j^2p_{j+1}-p_{j+1}^2p_j. \tag{87}$$

The slope and curvature at the middle point are obtained from

$$\tan\beta_j=\frac{(2ap_j+b)\cos\psi+\sin\psi}{-(2ap_j+b)\sin\psi+\cos\psi}, \tag{88}$$

$$R_j^{-1}=\frac{-2a}{[(2ap_j+b)^2+1]^{3/2}}. \tag{89}$$

The following differentiation rule is used to find the correction terms:

$$\Delta\mathcal{T}=\sum_{k=j-1}^{j+1}\frac{d\mathcal{T}}{dx_k}\Delta x_k+\frac{d\mathcal{T}}{dz_k}\Delta z_k, \tag{90}$$

$$\frac{d\mathcal{T}}{dx_k}=\frac{\partial\mathcal{T}}{\partial p_k}\cos\psi+\frac{\partial\mathcal{T}}{\partial a}\frac{\partial a}{\partial x_k}+\frac{\partial\mathcal{T}}{\partial b}\frac{\partial b}{\partial x_k}, \tag{91}$$

$$\frac{\partial(a,b)}{\partial x_k}=\frac{\partial(a,b)}{\partial p_k}\cos\psi+\frac{\partial(a,b)}{\partial q_k}\sin\psi, \tag{92}$$

where $\mathcal{T}$ is $\Delta\tan\beta$ or ΔR^{-1}. Introducing equation (34) to express Δx and Δz in terms of $\Delta\eta'$ yields the final form for the variations of the slope and the curvature:

$$\Delta\tan\beta_j=B_j^-\Delta\eta'_{j-1}+B_j^0\Delta\eta'_j+B_j^+\Delta\eta'_{j+1}, \tag{93}$$

where

$$B_j^-=\frac{d(\tan\beta)}{dx_{j-1}}\cos\gamma_{j-1}+\frac{d(\tan\beta)}{dz_{j-1}}\sin\gamma_{j-1},$$

$$B_j^0=\frac{d(\tan\beta)}{dx_j}\cos\gamma_j+\frac{d(\tan\beta)}{dz_j}\sin\gamma_j,$$

$$B_j^+=\frac{d(\tan\beta)}{dx_{j+1}}\cos\gamma_{j+1}+\frac{d(\tan\beta)}{dz_{j+1}}\sin\gamma_{j+1}, \tag{94}$$

and

$$\Delta R_j^{-1}=A_j^-\Delta\eta'_{j-1}+A_j^0\Delta\eta'_j+A_j^+\Delta\eta'_{j+1}, \tag{95}$$

where

$$A_j^- = \frac{\mathrm{d}(R^{-1})}{\mathrm{d}x_{j-1}} \cos\gamma_{j-1} + \frac{\mathrm{d}(R^{-1})}{\mathrm{d}z_{j-1}} \sin\gamma_{j-1},$$

$$A_j^0 = \frac{\mathrm{d}(R^{-1})}{\mathrm{d}x_j} \cos\gamma_j + \frac{\mathrm{d}(R^{-1})}{\mathrm{d}z_j} \sin\gamma_j,$$

$$A_j^+ = \frac{\mathrm{d}(R^{-1})}{\mathrm{d}x_{j+1}} \cos\gamma_{j+1} + \frac{\mathrm{d}(R^{-1})}{\mathrm{d}z_{j+1}} \sin\gamma_{j+1}. \tag{96}$$

The derivatives in (94) and (96) are calculated using (91) and (92).

APPENDIX III: TRUNCATION ERROR ANALYSIS

The boundary integral equation (16) is approximated to second-order in space when linear elements and shape functions and analytical integrations of equations (22)–(25) are used. The dynamic boundary condition (15) is approximated with two-point time and three-point spatial finite differences, the latter for $\partial\Phi/\partial s$. The leading errors are of order $(\theta - 0{\cdot}5)\Delta t$, $(\Delta t)^2$ and $(\Delta s)^2$. The kinematic boundary condition (14) is discretized in time only and the leading errors involve $(\theta - 0{\cdot}5)\Delta t$ and $(\Delta t)^2$. From test problems and an examination of coefficient derivatives, it appears that the leading errors generally arise from the dynamic boundary condition.[13]

The terms discretized in the dynamic boundary condition are contained essentially in the simplified equation

$$\frac{\partial\Phi}{\partial t} + \frac{1}{2}\left(\frac{\partial\Phi}{\partial s}\right)^2 = 0. \tag{97}$$

With the consistent method this is discretized as

$$\frac{\Phi_j^{k+1} - \Phi_j^k}{\Delta t} = -\frac{1}{2}\left\{(1-\theta)\left[\left(\frac{\partial\Phi}{\partial s}\right)_j^k\right]^2 + \theta\left[\left(\frac{\partial\Phi}{\partial s}\right)_j^k\left(\frac{\partial\Phi}{\partial s}\right)_j^{k+1}\right]\right\}, \tag{98}$$

where θ is the implicitness factor and $(\partial\Phi/\partial s)_j^k$ denotes the three-point finite difference approximation to the tangential derivative of the potential:

$$\left(\frac{\partial\Phi}{\partial s}\right)_j^k = C_j^+ \Phi_{j+1}^k + C_j^0 \Phi_j^k + C_j^- \Phi_{j-1}^k, \tag{99}$$

where the coefficients multiplying the potential are defined by (44). For comparison, an Eulerian–Lagrangian formulation would discretize (97) as

$$\frac{\Phi_j^{k+1} - \Phi_j^k}{\Delta t} = -\frac{1}{2}\left\{(1-\theta)\left[\left(\frac{\partial\Phi}{\partial s}\right)_j^k\right]^2 + \theta\left[\left(\frac{\partial\Phi}{\partial s}\right)_j^{k+1}\right]^2\right\}. \tag{100}$$

Note that the two formulations are linear and non-linear respectively in $(\partial\Phi/\partial s)_j^{k+1}$. Thus the Eulerian–Lagrangian formulation may require iteration over a time step but the consistent formulation does not, although the geometry at $k+1$ is respected by the method.

The modified equations corresponding to (98) and (100) are constructed by using double Taylor series expansions about time level $k+\theta$ and position j to replace each of the Φ-terms. The product terms on the right sides are not linearized. Each such term is replaced by products of series expansions. The modified equations which result contain derivatives in t which are replaced by derivatives in s only, using not the original partial differential equation (97) but the modified equations themselves.[14]

The modified equation corresponding to the consistent method, equation (98), is

$$\frac{\partial\Phi}{\partial t}+\frac{1}{2}\left(\frac{\partial\Phi}{\partial s}\right)^2=(\theta-\tfrac{1}{2})\Delta t\left(\frac{\partial\Phi}{\partial s}\right)^2\left(\frac{\partial^2\Phi}{\partial s^2}\right)$$
$$+(\Delta t)^2\left[(\tfrac{5}{2}\theta-2\theta^2-\tfrac{3}{4})\left(\frac{\partial^2\Phi}{\partial s^2}\right)^2+(\theta-\theta^2-\tfrac{1}{3})\frac{\partial\Phi}{\partial s}\frac{\partial^3\Phi}{\partial s^3}\right]\left(\frac{\partial\Phi}{\partial s}\right)^2$$
$$-\tfrac{1}{6}(\Delta s^k)^2\left\{1+\theta\left[\left(\frac{\Delta s^{k+1}}{\Delta s^k}\right)^2-1\right]\right\}\frac{\partial\Phi}{\partial s}\frac{\partial^3\Phi}{\partial s^3}+O(\Delta t^3,\Delta t\Delta s^2,\Delta s^3), \tag{101}$$

where all derivatives are evaluated at time level $k+\theta$ and position j. The modified equation corresponding to the Eulerian–Lagrangian formulation differs from (101) in the $(\Delta t)^2$-term, wherein $\frac{5}{2}\theta$ is replaced by 2θ. The two schemes are thus identical in their first-order time and second-order space truncation errors, but differ at terms $O(\Delta t^2)$ and higher.

REFERENCES

1. J. A. Liggett, 'Free surface flow—exposing the hidden nonlinearity', *Commun. Appl. Numer. Methods*, **4**, 509–516 (1988).
2. J. A. Liggett and P. L.-F. Liu, *The Boundary Integral Equation Method for Porous Media Flow*, Allen and Unwin, London, 1983.
3. M. S. Longuet-Higgins and E. D. Cokelet, 'The deformation of steep surface waves on water. I. A numerical method of computation', *Proc. R. Soc. Lond. A*, **350**, 1–26 (1976).
4. S. K. Kim, P. L.-F. Liu and J. A. Liggett, 'Boundary integral equation solutions for solitary wave generation, propagation, and run-up', *Coastal Eng.*, **7**, 299–317 (1983).
5. T. Nakayama and K. Washizu, 'The boundary element method applied to the analysis of two-dimensional nonlinear sloshing problems', *Int. j. numer. methods eng.*, **17**, 1631–1646 (1982).
6. J. W. Dold and D. H. Peregrine, 'Steep unsteady water waves, an efficient computational scheme', *Proc. 19th Coastal Engineering Conf., Vol. 1*, Houston, 1984, ASCE, pp. 955–967.
7. D. G. Dommermuth and D. K. P. Yue, 'Numerical simulations of nonlinear axisymmetric flows with a free surface', *J Fluid Mech.*, **178**, 195–219 (1987).
8. D. E. Medina, 'Advanced applications of the boundary element method to ground water flow in fractured rock and free surface hydrodynamics', *Ph.D. Dissertation*, Civil and Environmental Engineering, Cornell University, Ithaca, NY, 1989.
9. J. L. Hammack, 'A note on tsunamis: their generation and propagation in an ocean of uniform depth', *J. Fluid Mech.*, **60**, 769–799 (1973).
10. C. C. Mei, *The Applied Dynamics of Ocean Surface Waves*, Wiley, New York, 1983.
11. N. Sugimoto, Y. Kusaka and T. Kakutani, 'Reflection of a shallow-water soliton. Part 2. Numerical evaluation', *J. Fluid Mech.*, **178**, 99–117 (1987).
12. W. G. Penney and A. T. Price, 'Finite periodic stationary gravity waves in a perfect liquid', *Phil. Trans. R. Soc. Lond., Ser. A*, **244**, 254–284 (1952).
13. R. A. Birchwood and K. E. Torrance, 'Truncation error analysis of a boundary element method for free surface flow', *Report E-89-05*, Sibley School of Mechanical and Aerospace Engineering, Cornell University, Ithaca, NY, 1989.
14. D. A. Anderson, J. C. Tannehill and R. H. Pletcher, *Computational Fluid Mechanics and Heat Transfer*, Hemisphere, Washington, DC, 1984.